Validation studies of gyrokinetic ITG and TEM turbulence simulations in JT-60U tokamak using multiple flux matching

Motoki Nakata[1]**, Mitsuru Honda**[2]**, Maiko Yoshida**[2]**, Hajime Urano**[2]**, Masanori Nunami**[1]**, Shinya Maeyama**[3]**, Tomo-Hiko Watanabe**[3]**, and Hideo Sugama**[1]

[1] National Institute for Fusion Science, Toki 509-5292, Japan

[2] National Institutes for Quantum and Radiological Science and Technology, Naka 311-0193, Japan

[3] Department of Physics, Nagoya University, Nagoya 464-8602, Japan

E-mail: `nakata.motoki@nifs.ac.jp`

Abstract. Quantitative validation studies of flux-tube gyrokinetic Vlasov simulations on ion and electron heat transport are carried out for the JT-60U tokamak experiment. Ion temperature gradient (ITG) and/or trapped electron modes (TEM) driven turbulent transport and zonal flow generations are investigated for an L-mode plasma in the local turbulence limit with sufficiently small normalized ion thermal gyroradius and weak mean radial electric fields. Nonlinear turbulence simulations by the GKV code successfully reproduce radial profiles of the ion and electron energy fluxes in the core region. The numerical results show that the TEM-driven zonal flow generation in the outer region is more significant than that in the core region with ITG- and ITG-TEM-dominated turbulence, leading to moderate transport shortfall of the ion energy flux. Error levels in prediction of the ion and electron temperature gradient profiles in the core region are estimated as less than ±30%, based on a multiple flux matching technique, where the simulated ion and electron energy fluxes are simultaneously matched to the experimental values.

1. Introduction

Performance of particle and energy confinement in magnetic fusion plasmas is mainly influenced by turbulent transport driven by electrostatic and electromagnetic microinstabilities. Physical understanding and quantitative prediction of the turbulent transport are central issues in fusion plasma researches. The five-dimensional nonlinear turbulence simulation based on the gyrokinetic theory [see e.g., Refs. [1, 2] and references therein] is widely recognized as a promising way to address the turbulent transport issues, and one can find comprehensive reviews on the gyrokinetic simulations in Refs. [3, 4]. Great efforts have been devoted so far to development of the radially local simulation approaches and its extensions to global model, and then the ion temperature gradient (ITG) and the trapped electron mode (TEM) driven turbulent transport has been extensively investigated. Systematic cross-code benchmark tests have confirmed that the ITG driven turbulent heat transport level in the global simulation well converges to the local flux-tube one in a limit of sufficiently small ion thermal gyroradius (ρ_{ti}) compared to the plasma size (a) and/or the characteristic profile width of the logarithmic ion temperature gradient ($\Delta_{\nabla \ln T_i}$), i.e., $\rho^* = \rho_{ti}/a < 1/300$ or $\rho^*_{eff} = \rho_{ti}/\Delta_{\nabla \ln T_i} < 1/300$ [7, 8]. The local gyrokinetic simulations are, therefore, well applicable to the the next-generation large tokamak devices such as ITER and DEMO with $\rho^* < 1/500$, and the evaluation of their prediction capability through quantitative comparisons with the existing plasma experiments is a crucial requirement.

In the last decade, validation studies of gyrokinetic simulation codes have been actively carried out for various tokamak (e.g., DIII-D [9, 10, 11, 12], ASDEX Upgrade [13], Alcator C-MOD [14], etc.) and helical (e.g., LHD [15, 16]) devices. In the tokamak validation studies, a significant underprediction of the heat flux, which is the so-called "transport shortfall" [10], has been identified in the outer region around $\rho = r/a \geqslant 0.7$, and the numerical and physical effects on the transport shortfall are investigated for the DIII-D L-mode plasma as a representative case [9, 11, 17]. Particularly, Görler et al. has recently pointed out that the significant ion transport shortfall is resolved within the measurement errors of the ion temperature gradient, based on the flux matching technique [18], taking into account the stiff dependence of the turbulent heat flux on the ion temperature gradient [11]. Also, the strong impact of the mean radial electric field shearing on the simulated ion heat flux has been confirmed.

On the other hand, characteristics of the ITG and/or TEM driven zonal flows, which depend on the radial position in the L-mode plasma, and the relation with the transport shortfall have not been investigated in earlier works. Indeed, since the transport suppression by zonal flows is expected to be more significant in the future large tokamaks such as ITER than the mean radial electric field shear which is roughly proportional to ρ^*, gyrokinetic-simulation-based studies of the zonal flow properties are indispensable for improving the

prediction capability. As a fundamental study on the nonlinear interactions of zonal flows and turbulence, the gyrokinetic entropy transfer analyses have been carried out for the ITG, TEM, and ETG turbulence [19, 20, 21, 22].

In this paper, the first quantitative validation study on the ion and electron heat transport including the zonal flow analysis for a JT-60U tokamak plasma is presented. Here, the JT-60U L-mode discharge is carefully chosen such that the local limit condition of $\rho_i^* < 1/300$ is well satisfied, i.e., the mean radial electric field shearing rate is negligibly small in comparison to the linear-mode growth rate. The nonlinear ITG and/or TEM turbulence simulations under the experimental conditions are performed by using an electromagnetic gyrokinetic Vlasov code GKV [23, 24]. Then, the experimental equilibrium profiles, power and particle balances are provided by an integrated tokamak transport solver TOPICS [25, 26]. Furthermore, the conventional ion heat flux matching by adjusting a single parameter of the ion temperature gradient [11] is extended to a multiple flux matching associated with the nonlinear dependence on the ion and electron temperature gradients, where the simulated ion and electron energy fluxes are simultaneously matched to the experimental values. Then, we evaluate the accuracy of the temperature-gradient profile prediction in the core region.

The rest of the paper is organized as follows. The calculation model in GKV under the experimental condition produced by TOPICS is presented in Sec. 2. Then, plasma parameters, equilibrium profiles, and the linear instabilities of the present L-mode plasma are shown in Sec. 3. In Sec. 4, nonlinear simulation results on the ITG and/or TEM driven turbulent transport and zonal flows at several radial positions are presented. The quantitative comparisons with the experimental results and the multiple flux matching are discussed. Finally, a summary of this paper is given in Sec. 5.

2. Calculation model

2.1. Flux-tube gyrokinetic simulation model for realistic tokamak equilibria

In this section, we briefly summarize the gyrokinetic simulation model used in the electromagnetic gyrokinetic Vlasov code GKV and an interface with the integrated tokamak transport solver TOPICS providing the experimental equilibrium profiles. The detailed descriptions are also given in Ref. [24]. One of the governing equations is the electromagnetic gyrokinetic equation describing the time evolution of the perturbed gyrocenter distribution function $\delta f_s^{(g)}$ on the five-dimensional phase-space $(\boldsymbol{x}_g, v_\parallel, \mu)$, where the subscript "s" is the index of particle species. The Fourier representation with the perpendicular wavenumber $\boldsymbol{k}_\perp$ is given by

$$\left(\frac{\partial}{\partial t} + v_\parallel \boldsymbol{b}\cdot\nabla + i\omega_{\mathrm{Ds}} - \frac{\mu \boldsymbol{b}\cdot\nabla B}{m_\mathrm{s}}\frac{\partial}{\partial v_\parallel}\right)\delta g_{s\boldsymbol{k}_\perp} - \frac{c}{B}\sum_\Delta \boldsymbol{b}\cdot(\boldsymbol{k}_\perp' \times \boldsymbol{k}_\perp'')\,\delta\psi_{s\boldsymbol{k}_\perp'}\delta g_{s\boldsymbol{k}_\perp''}$$

$$= \frac{e_\mathrm{s}F_{\mathrm{Ms}}}{T_\mathrm{s}}\left(\frac{\partial\delta\psi_{\boldsymbol{k}_\perp}}{\partial t} + i\omega_{*Ts}\delta\psi_{\boldsymbol{k}_\perp}\right) + C_\mathrm{s}(\delta g_{s\boldsymbol{k}_\perp})\ , \tag{1}$$

where $\delta g_{s\boldsymbol{k}_\perp}$ stands for the non-adiabatic part of the perturbed gyrocenter distribution function $\delta f_{s\boldsymbol{k}_\perp}^{(g)}$, i.e., $\delta g_{s\boldsymbol{k}_\perp} = \delta f_{s\boldsymbol{k}_\perp}^{(g)} + e_\mathrm{s}J_{0\mathrm{s}}\delta\phi_{\boldsymbol{k}_\perp}F_{\mathrm{Ms}}/T_\mathrm{s}$. The particle mass, the electric charge, the

equilibrium temperature, and the gyrofrequency are denoted by m_s, e_s, T_s, and $\Omega_s = e_s B/m_s c$, respectively. The parallel velocity $v_\parallel$ and the magnetic moment μ are used as the velocity-space coordinates, where μ is defined by $\mu = m_s v_\perp^2/2B$ with the perpendicular velocity $v_\perp$. The gyro-averaged potential fluctuation is denoted by $\delta\psi_{\boldsymbol{k}_\perp} := J_{0s}[\delta\phi_{\boldsymbol{k}_\perp} - (v_\parallel/c)\delta A_{\parallel \boldsymbol{k}_\perp}]$, where $J_{0s} := J_0(k_\perp v_\perp/\Omega_s)$ is the zeroth-order Bessel function, and the former and latter terms mean the electrostatic and electromagnetic parts, respectively. Since we focus here on the finite but low-β L-mode plasmas, the parallel magnetic field fluctuation $\delta B_{\parallel \boldsymbol{k}_\perp}$ (so called the compressional component) is ignored. The equilibrium part of the distribution function is given by the local Maxwellian distribution, i.e., $F_{Ms} = n_s(m_s/2\pi T_s)^{3/2}\exp[-(m_s v_\parallel^2 + 2\mu B)/2T_s]$, where n_s represents the equilibrium density. The symbol $\sum_\Lambda$ appearing in the nonlinear term of Eq. (1) means the double summations with respect to $\boldsymbol{k}_\perp'$ and $\boldsymbol{k}_\perp''$, which satisfy the triad-interaction condition of $\boldsymbol{k}_\perp = \boldsymbol{k}_\perp' + \boldsymbol{k}_\perp''$. Collisional effects are introduced in terms of a linearized model collision operator C_s, where a gyro-averaged Lenard-Bernstein model [27] is applied here.

The gyrokinetic equation shown in Eq. (1) is solved in the local flux-tube coordinates (x, y, z) [28] defined as $x = a(\rho - \rho_0)$, $y = a\rho_0 q(\rho_0)^{-1}[q(\rho)\theta - \zeta]$, $z = \theta$ with the straight field line coordinates (ρ, θ, ζ), where a and $q(\rho_0)$ denote the plasma minor radius and the safety factor on the flux surface label of interest ρ_0, respectively. In these coordinates, the magnetic field vector is given by $\boldsymbol{B} = B_{ax}\nabla x \times \nabla y$ with the field strength on the magnetic axis B_{ax}. The perpendicular wavenumber vector and the parallel derivative operator are given as $\boldsymbol{k}_\perp = k_x \nabla x + k_y \nabla y$, $\boldsymbol{b} \cdot \nabla = (B_{ax}/B\sqrt{g_{xyz}})\partial/\partial z$, where $\sqrt{g_{xyz}} = \det(g^{ij})^{-1/2}$ is the Jacobian given by the contravariant components of the metric tensor g^{ij} for $(i, j) = (x, y, z)$. The magnetic and diamagnetic drift frequencies, ω_{Ds} and ω_{*Ts}, are then given by

$$
\begin{aligned}
\omega_{Ds} &= \frac{c}{e_s B}\boldsymbol{k}_\perp \cdot \boldsymbol{b} \times \left(\mu\nabla B + m_s v_\parallel^2 \boldsymbol{b}\cdot\nabla\boldsymbol{b}\right) \\
&= \frac{c(m_s v_\parallel^2 + \mu B)}{e_s B_{ax}}\left(\mathcal{K}_x k_x + \mathcal{K}_y k_y\right) ,
\end{aligned}
\tag{2}
$$

$$
\begin{aligned}
\omega_{*Ts} &= \frac{cT_s}{e_s B}\left[1 + \eta_s\left(\frac{m_s v_\parallel^2 + 2\mu B}{2T_s} - \frac{3}{2}\right)\right]\boldsymbol{k}_\perp \cdot \boldsymbol{b} \times \nabla\ln n_s \\
&= -\frac{cT_s}{e_s B_{ax}}\left[\frac{1}{L_{n_s}} + \frac{1}{L_{T_s}}\left(\frac{m_s v_\parallel^2 + 2\mu B}{2T_s} - \frac{3}{2}\right)\right]k_y ,
\end{aligned}
\tag{3}
$$

where $\eta_s = L_{n_s}/L_{T_s}$ with $L_{n_s} = -(d\ln n_s/dx)^{-1}$ and $L_{T_s} = -(d\ln T_s/dx)^{-1}$. The geometric coefficients $\mathcal{K}_x$ and $\mathcal{K}_y$ are defined as follows:

$$
\mathcal{K}_x = \frac{g^{xz}g^{xy} - g^{xx}g^{yz}}{B^2/B_{ax}^2}\frac{\partial \ln B}{\partial z} - \frac{\partial \ln B}{\partial y} ,
\tag{4}
$$

$$
\mathcal{K}_y = \frac{g^{xz}g^{yy} - g^{xy}g^{yz}}{B^2/B_{ax}^2}\frac{\partial \ln B}{\partial z} + \frac{\partial \ln B}{\partial x} .
\tag{5}
$$

Note that the low-β approximation is applied to ω_{Ds} so that the finite-β effect is ignored in the curvature drift.

The electromagnetic potential fluctuations are determined by the Poisson and Ampère

equations:

$$\left(k_\perp^2 + \lambda_D^{-2}\right)\delta\phi_{\boldsymbol{k}_\perp} = 4\pi \sum_s e_s \int d\boldsymbol{v} J_{0s}\delta g_{s\boldsymbol{k}_\perp} , \tag{6}$$

$$k_\perp^2 \delta A_{\|\boldsymbol{k}_\perp} = \frac{4\pi}{c} \sum_s e_s \int d\boldsymbol{v}\, v_\| J_{0s}\delta g_{s\boldsymbol{k}_\perp} , \tag{7}$$

where $\lambda_D = (\sum_s 4\pi n_s e_s^2/T_s)^{-1/2}$ is the Debye length. The charge neutrality in the background density n_s is described as $\sum_{s\neq e} f_{Cs} = 1$, where $f_{Cs} \equiv Z_s n_s/n_e$ means the charge-density fraction for ions with the charge number Z_s. The source term for each species in the right of Eqs. (6) and (7) are proportional to f_{Cs}. In addition, the radial derivative of the above charge neutrality condition leads to another constraint for the background density gradient, i.e., $\sum_{s\neq e} f_{Cs}L_{n_s}^{-1} = L_{n_e}^{-1}$. It is also noted that, in the adiabatic electron limit with $k_\perp\rho_{te} \ll 1$, the gyrocenter density fluctuation for electrons is approximated by $\int d\boldsymbol{v}\,\delta f^{(g)}_{e\boldsymbol{k}_\perp} \simeq -en_e(\delta\phi_{\boldsymbol{k}_\perp} - \langle\delta\phi_{\boldsymbol{k}_\perp}\rangle_z \delta_{k_y,0})/T_e$, where $\rho_{ts} = m_s c v_{ts}/|e_s|B_{ax}$ means the gyroradius evaluated with the thermal speed $v_{ts} = (T_s/m_s)^{1/2}$, and the field-line average is defined by $\langle X_{\boldsymbol{k}_\perp}\rangle_z = \int dz\sqrt{g_{xyz}}X_{\boldsymbol{k}_\perp}/\int dz\sqrt{g_{xyz}}$.

By using the gyrokinetic and the Poisson-Ampère equations, one can derive another important equation describing the balance and transfer of the entropy variable $\delta S_{s\boldsymbol{k}_\perp} \equiv \langle\int d\boldsymbol{v}\,|\delta f_{\boldsymbol{k}_\perp}|^2/2F_{Ms}\rangle_z$ defined with the particle (not gyrocenter here) distribution function $\delta f_{\boldsymbol{k}_\perp} = -e_s\delta\phi_{\boldsymbol{k}_\perp}F_{Ms}/T_s + \delta g_{s\boldsymbol{k}_\perp}e^{-i\boldsymbol{k}_\perp\cdot\boldsymbol{\rho}_s}$,

$$\sum_s \left(\underbrace{\frac{d}{dt}T_s\delta S_s^{(trb)}}_{(i)} \underbrace{+T_s\delta R_s^{(trb)}}_{(ii)} \underbrace{+T_s\mathcal{J}_s^{(zf)}}_{(iii)} \underbrace{-T_s\Omega_s^{(trb)}}_{(iv)} \underbrace{-T_s D_s^{(trb)}}_{(v)}\right) = 0 , \tag{8}$$

$$\sum_s \left(\underbrace{\frac{d}{dt}T_s\delta S_s^{(zf)}}_{(i)} \underbrace{+T_s\delta R_s^{(zf)}}_{(ii)} \underbrace{-T_s\mathcal{J}_s^{(zf)}}_{(iii)} \underbrace{-T_s D_s^{(zf)}}_{(v)}\right) = 0 , \tag{9}$$

where the superscripts "(trb)" and "(zf)" mean the non-zonal and zonal components in the wavenumber space, respectively, i.e., $X^{(trb)} \equiv \sum_{k_x}\sum_{k_y\neq 0} X_{k_x,k_y}$, $X^{(zf)} \equiv \sum_{k_x} X_{k_x,k_y=0}$. Each term represents (i) the variation of the entropy variable, (ii) the variation of the field energy, (iii) the nonlinear entropy transfer from non-zonal to zonal modes, (iv) the entropy production by turbulent particle and heat fluxes, and (v) the collisional dissipation, respectively (see, e.g., Ref. [29] for their definitions). Note that, by the definition, the turbulent-flux driven entropy production term does not appear for the zonal modes in Eq. (9). The entropy balance/transfer equation provides us with a good measure for the turbulence simulation accuracy as well as useful physical insights associated with the turbulence saturation mechanisms. The detailed numerical analyses of the entropy balance and the transfer processes in ITG, TEM, and ETG turbulence are shown in, e.g., Refs. [20, 21, 22, 23].

2.2. Interface with integrated-transport solver

In this section, we present the framework of combined analyses by means of GKV and the integrated-transport solver TOPICS with experimental density and temperature profiles and

magnetic fields. In GKV, effects of magnetic field geometries are incorporated into the field intensity B, the parallel derivative $\boldsymbol{b}\cdot\nabla$, the magnetic drift ω_{Ds}, the perpendicular wavenumber $k_\perp$, and the field-line-average operator $\langle\cdots\rangle_z$ shown in Sec. 2.1, through the contravariant components of metric tensor g^{ij} and the Jacobian $\sqrt{g}_{xyz}$.

Figure 1 shows a schematic procedure to make the realistic MHD equilibrium data for turbulence simulations with GKV. First, the MHD equilibrium based on the experimentally measured density, temperature, and current profiles is reconstructed by TOPICS. The radial profiles of the ion and electron energy fluxes are simultaneously provided by the power balance analysis for e.g., Ohmic, NBI, and EC heatings, where the power depositions and losses are calculated by a fast-ion orbit following Monte-Carlo Fokker-Planck solver OFMC [25, 30]. After that, a flux coordinate generator IGS [24] makes high-accuracy interpolations of the flux surfaces and constructs the straight-field-line coordinates, such as the axisymmetric (or natural), Boozer, and Hamada coordinates. Using these coordinates data, the metric tensor and the Jacobian for geometry-dependent quantities and operators are calculated in GKV. It is noted that the up-down asymmetry resulting from the divertor configuration is consistently included in this framework.

The combined analyses among GKV and TOPICS via IGS enable us to make not only experimental analyses, but also predictive studies for future devices, e.g., shape optimization on the microinstability and turbulent transport. Actually, in Ref. [24], GKV with realistic tokamak equilibria is numerically verified through the cross-code benchmark test. It is, then, applied to two types of shaped plasmas expected in the JT-60SA tokamak device, i.e., ITER-like and highly-shaped plasmas, where decrease in the ITG-mode growth rate and enhancement of the residual zonal flow level in the highly-shaped case are identified.

3. JT-60U L-mode equilibrium and linear instability analyses

Using the framework of GKV-TOPICS, gyrokinetic simulation studies for the JT-60U tokamak experiments are carried out. Then, the prediction capability of GKV is examined through comparisons between the simulation and experimental results on the turbulent ion and electron energy fluxes. For a validation study of the local flux-tube gyrokinetic simulation, we have chosen a JT-60U deuterium plasma on the L-mode discharge with a positive magnetic shear profile [31], where $\rho^* \simeq 1/500$ and $\rho^*_{\mathrm{eff}} \equiv \rho_{\mathrm{ti}}/L_{T_{\mathrm{i}}} \simeq 1/400$ for $\rho < 0.8$ well satisfy the local limit condition of $\rho^* < 1/300$ [5, 6, 7, 8]. The configuration parameters of the experiment are summarized in Tab. 1.

The plasma shape and equilibrium profiles are shown in Figs. 2. It is noted that the electron temperature is slightly higher than the ion one for $\rho \leqslant 0.7$. The mean toroidal rotation and the mean poloidal $E \times B$ rotation are negligibly small in the whole radial region, i.e., $|U_{\mathrm{tor}}| \sim 0.1 v_{\mathrm{ti}}$ and $|U_{E \times B}| \sim 0.1 v_{\mathrm{ti}}\epsilon/q$, One also finds almost monotonically increasing profiles of the normalized density/temperature gradient, $R_{\mathrm{ax}}/L_{n_{\mathrm{e}}}$, $R_{\mathrm{ax}}/L_{T_{\mathrm{i}}}$, and $R_{\mathrm{ax}}/L_{T_{\mathrm{e}}}$. The normalized collisionality $\nu^*_{\mathrm{ss'}}$ is around 0.1 (banana-plateau regime) for both ion-ion and electron-electron collisions, where the definition is given by $\nu^*_{\mathrm{ss'}} = qR_{\mathrm{ax}}\tau^{-1}_{\mathrm{ss'}}/(\sqrt{2}\epsilon^{3/2}v_{\mathrm{ts}})$ with the characteristic collision time $\tau_{\mathrm{ss'}}$. Besides, the mean radial electric field shearing rate γ_{E_r} is about 10 times

Table 1. Configuration parameters in JT-60U L-mode plasma: #E45072

R_{ax} [m]	a [m]	V [m^3]
3.37	1.03	66.6
B_{ax} [T]	I_p [MA]	q_{95}
2.61	1.16	3.87
β_i on axis [%]	$P_{NB}^{(aux)}$ [MW]	$P_{Ohmic}^{(aux)}$ [MW]
0.28	1.42	0.64

smaller than the linear-mode growth rate γ_{lin}. The local simulation approach is, thus, well justified for the plasma investigated here.

The wavenumber dependence of the linear instability growth rate $\gamma_{lin}(k_y)$ calculated by the linear GKV simulations is shown in Figs. 3, where $\gamma_{lin}(k_y)$ for three radial positions, $\rho = 0.26,\ 0.50,\ 0.76$ are plotted. Since, as shown in Fig. 2(g), the normalized gradients rapidly increase towards the plasma edge, the different linear microinstabilities appear at each radial position, where the ITG, ITG-TEM, and TEM instabilities are dominant in the ion-scale modes of $k_y\rho_{ti} \leqslant 2$ at $\rho = 0.26,\ 0.50,\ 0.76$, respectively. The ETG modes are also unstable at $\rho = 0.50$ and 0.76. The ITG- and ETG-mode growth rates calculated with adiabatic electrons or ions are also plotted. One can see that the adiabatic-electron approximation is only valid in the deep core region ($\rho \sim 0.26$) where fraction of the trapped electrons becomes less significant in comparison to that in the outer region. It is also noteworthy that the maximum growth rate in the ion-scale modes with $k_y\rho_{ti} < 1$ increases towards the outer region.

4. ITG and/or TEM driven turbulence simulations

4.1. Numerical settings and the entropy balance relations

Turbulence simulation results and comparisons with the experimental measurements are discussed in this section. The ITG and/or TEM turbulence simulations at several points in $0.26 \leqslant \rho \leqslant 0.76$ are carried out. Here, $\rho = 0.76$ is chosen as the maximum radial position, following the baseline position of the transport shortfall in DIII-D case considered in the earlier works [9, 10, 11, 12]. Only ion-scale electromagnetic fluctuations of $k_{y(max)}\rho_{ti} \leqslant 2$ are solved. The linearly stable region for $k_x\rho_{ti} > 1$ and the finite collisions lead to the statistically steady turbulence state even when any numerical dissipations are not imposed in the higher k_y region. The pure deuterium-electron plasma without any impurity ions is considered here. As for the numerical resolution, (168,32)-mode numbers in (k_x, k_y) and (64,64,32)-grid numbers in $(z, v_\parallel, v_\perp)$ are used, where the velocity-space domain is taken with $(v_\parallel|_{max}, v_\perp|_{max}) = (5v_{ts}, 5v_{ts})$ for s = i, e at $z = 0$. As shown in Figs. 4(a) and 4(b), the entropy balance relations for both the non-zonal (turbulent) and zonal components are accurately satisfied in the present turbulence simulations, where the labeling number for each line corresponds to the term in the left hand side of Eqs. (8) and (9), respectively.

4.2. Comparisons of turbulence simulation results with experimental measurements

The simulation results on the turbulent energy fluxes for ions and electrons are compared with experimental measurements. Figures 5 show the spectro-temporal evolutions of the radial turbulent energy flux density $Q_{ik_\perp}/Q_{\rm GBi}$ and $Q_{ek_\perp}/Q_{\rm GBi}$ at $\rho = 0.26$, 0.50, 0.76 calculated by GKV, where $Q_{sk_\perp} = -(c/B){\rm Re}\int d\boldsymbol{v}\,(m_s v^2/2)ik_y\delta\psi_{k_\perp}\delta g^*_{sk_\perp}$. Both the ion and electron energy fluxes in the quasi-steady state of $t > 80R_{\rm ax}/v_{\rm ti}$ are dominated by low wavenumber modes of $k_y\rho_{\rm ti} < 0.5$ in the ITG-TEM and TEM cases even with the wide unstable wavenumber region expanding beyond $k_y\rho_{\rm ti} \sim 1$. Indeed, the wavenumber at the spectral peak is similar to or lower than that giving the maximum linear growth rate (shown by the horizontal dashed line in the contours). It is also found that contribution of the higher-wavenumber modes is more significant for the electron energy flux, where the amplitude $|Q_{ek_\perp}|$ is about 10 times larger than that $|Q_{ik_\perp}|$ for $k_y\rho_{\rm ti} \sim 2$.

The radial dependencies of the turbulence part $W_{\rm trb}$ with $k_y \neq 0$ and the zonal flow part $W_{\rm zf}$ with $k_y = 0$ in the generalized flow energy $W_{\rm total}$ are shown in Figs. 6(a) and 6(b), where $W_{\rm total}$ is defined by $W_{\rm total} = \langle\sum_{\boldsymbol{k}_\perp}\sum_{\rm s}(n_s e_s^2/2T_s)(1-\Gamma_{0s})|\delta\phi_{\boldsymbol{k}_\perp}|^2\rangle_z \simeq \langle\sum_{\boldsymbol{k}_\perp}(n_i e_i^2/2T_i)k_\perp^2\rho_{\rm ti}^2|\delta\phi_{\boldsymbol{k}_\perp}|^2\rangle_z$, and the quantities are time-averaged over the steady turbulence state. For comparisons, the mixing-length estimate of diffusivity, i.e., $\max[\gamma_{\rm lin}/k_y^2]$, and the normalized entropy transfer rate for the zonal modes $\mathcal{J}_i^{({\rm zf})}/(L_{T_i}^{-1}Q_i/T_i)$ representing the nonlinear source for the zonal flow generation are also plotted in the figures. We see that the monotonic increase in the turbulence energy $W_{\rm trb}$ is well correlated with the mixing-length estimate. As for the zonal flow energy normalized by the turbulence part $W_{\rm zf}/W_{\rm trb}$, a weak radial dependence is found for the core region of $\rho \leqslant 0.50$ indicating the ITG- and ITG-TEM-dominated turbulence, while more significant zonal flow generation is observed for the outer region with TEM-dominated turbulence. This is consistent with the tendency of the entropy transfer rate in Fig. 6(b). The understanding of the correlation among the turbulence energy, zonal flow energy, and the entropy transfer rate is useful for constructing a simplified turbulent transport model [15] which can be applied to the integrated transport simulations [32].

Figures 7 show the comparisons between GKV simulation results and experimental measurements on the radial profiles of the ion energy flux P_i, the electron energy flux P_e, and the convective part resulting from the turbulent particle flux $(5/2)T_e\Gamma_e$ in the unit of MW. The flux-surface-integrated radial energy and particle fluxes are defined as $P_s = \int d\theta d\zeta\sqrt{g}\,\boldsymbol{Q}_s\cdot\nabla\rho = \langle Q_s^\rho\rangle_{\rm fs}V'(\rho)$ and $\Gamma_s = \int d\theta d\zeta\sqrt{g}\,\boldsymbol{\Gamma}_s\cdot\nabla\rho = \langle\Gamma_s^\rho\rangle_{\rm fs}V'(\rho)$, where Q_s^ρ and Γ_s^ρ mean the contravariant radial components of the energy and particle flux density vectors (in the unit of MW/m^3) given by $\boldsymbol{Q}_s = (c/B)\int d\boldsymbol{v}\,(m_s v^2/2)\,\delta g_s\boldsymbol{b}\times\nabla_\perp\delta\phi$, $\boldsymbol{\Gamma}_s = (c/B)\int d\boldsymbol{v}\,\delta g_s\boldsymbol{b}\times\nabla_\perp\delta\phi$, respectively. The flux-surface average is denoted by $\langle\cdots\rangle_{\rm fs}$. The experimental values, $P_{\rm i(EXP)}$ and $P_{\rm e(EXP)}$ are evaluated by the steady power balance analysis with TOPICS. The definition is given by $P_{\rm s(EXP)} = \langle\mathcal{S}_s\rangle_{\rm fs}V'(\rho)$, where the source/sink deposition terms $\mathcal{S}_s$ for ions (s=i) and electrons (s=e) are given by $\mathcal{S}_e = \mathcal{S}_{\rm Ohmic} + \mathcal{S}_{\rm e(NB)} + \mathcal{S}_{\rm eq(i\to e)} - \mathcal{S}_{\rm rad}$, $\mathcal{S}_i = \mathcal{S}_{\rm i(NB)} - \mathcal{S}_{\rm eq(i\to e)} - \mathcal{S}_{\rm CX}$, respectively. Here, each term means the contribution from the Ohmic heating ($\mathcal{S}_{\rm Ohmic}$), NBI heating ($\mathcal{S}_{\rm s(NB)}$), collisional equipartition ($\mathcal{S}_{\rm eq(i\to e)}$), radiation loss ($\mathcal{S}_{\rm rad}$), charge exchange loss ($\mathcal{S}_{\rm CX}$). Note that the radiation loss is not taken into account in this analysis. For comparisons,

the results with the adiabatic-electron ("ad.-elec.") approximation and with a gyrofluid-based transport model TGLF [33] are also plotted. Note that, since the L-mode plasma chosen here shows negligibly small radial electric fields [cf. Fig. 2(e)], weak impact of the radial $E \times B$ shearing effect is confirmed in the TGLF cases. One finds that the GKV simulations with kinetic electrons reproduce transport levels relevant to the experimental measurements in the core region ($\rho \leqslant 0.50$) for both the ion and electron energy fluxes, whereas the adiabatic electron case predicts lower transport levels. Also, TGLF and GKV results show similar energy transport levels for the ITG-dominated region of $\rho \leqslant 0.4$, but some differences are found in outer region with the TEM-dominated turbulence. As for the particle flux Γ_e, slightly lower transport level is found in the GKV results, but still the same order of magnitude in comparison to that in the TGLF cases. Note that the experimental evaluation of Γ_e is not available due to large uncertainty in the particle source and sink depositions which are strongly influenced by the particle recycling and the ionization/recombination processes in the plasma edge.

It is stressed that the ion energy flux in GKV decreases towards the outer region of $\rho > 0.50$ despite the monotonically increasing tendency of the linear growth rate shown in Fig. 6(a). Indeed, the stronger zonal flow generation from the TEM turbulence is associated with the transport reduction in the outer region. Consequently we see a moderate transport shortfall with relatively larger deviations from the experimental value for P_i in comparison to those in the core region of $\rho \leqslant 0.50$. The parameter sensitivity of the transport shortfall associated with the strong zonal flows are discussed in Sec. 4.3, as well as the flux matching evaluation of the profile prediction accuracy.

4.3. Ion and electron temperature gradient dependencies and multiple flux matching

As pointed out in Ref. [11], since the experimental plasmas often show a stiff response of temperature profiles against the auxiliary heating, the sensitivity of the calculated turbulent fluxes on the equilibrium profiles should be examined to make more robust validation. In this section, we discuss dependencies of the turbulence simulation results on the numerical and physical parameters. Also, in the later part, the flux matching technique is applied for both P_i and P_e simultaneously to evaluate the prediction accuracy of the ion and electron temperature gradient profiles.

The numerical convergence with respect to the maximum wavenumber is shown in Figs. 8, where influences of the faster and finer TEM-unstable fluctuations [Fig. 8(a)] are examined for the time evolution of ion and electron energy fluxes at $\rho = 0.50$ [Fig. 8(b)] and $\rho = 0.76$ [Fig. 8(c)]. We see that the higher maximum wavenumber leads to faster linear growth of the TEM modes for both cases. Their growths, then, saturate at much lower levels than that after the saturation of the ITG-mode growth. Thus, the mean saturation levels of P_i and P_e in the steady state are not affected by the TEM modes with higher k_y. This is also consistent with the fact that the lower wavenumber modes are dominant in the turbulent energy fluxes shown in Figs. 5.

The temperature-gradient dependencies of the ion energy flux P_i, the electron energy

flux P_{e}, the turbulence energy W_{trb}, and the zonal flow energy W_{zf} (normalized by the total one $W_{\text{total}} = W_{\text{trb}} + W_{\text{zf}}$) in the ITG ($\rho = 0.30$), ITG-TEM ($\rho = 0.50$), and TEM ($\rho = 0.76$) dominated regimes are summarized in Figs. 9(a) – 9(c). Note that the variable $L_{T_{\text{s}}}^{-1}$ (s = i, e) in the horizontal axis is normalized by the experimental mean value $L_{T_{\text{s(EXP)}}}^{-1}$ as shown in Fig. 1(g), and $X_{\text{(ref)}}$ means the reference simulation results of $X = \{P_{\text{i}},\ P_{\text{e}},\ \Gamma_{\text{e}},\ W_{\text{trb}},\ W_{\text{zf}}/W_{\text{total}}\}$ in terms of $L_{T_{\text{s(EXP)}}}^{-1}$. Reflecting the interplay of turbulence, zonal flows and the resultant fluxes, each temperature-gradient dependence is somewhat complicated. However, we can see clear overall tendency that magnitude of the temperature-gradient dependence becomes weak towards the outer region. Actually, $|\partial X/\partial L_{T_{\text{s}}}^{-1}|$ in the TEM-dominated region of $\rho = 0.76$ is much smaller than that in the ITG-dominated region of $\rho = 0.30$. It is also stressed that P_{i} and P_{e} indicate different $L_{T_{\text{i}}}^{-1}$- and $L_{T_{\text{e}}}^{-1}$-dependencies, which are crucial to apply a multiple flux matching technique shown below.

In the present local flux-tube delta-f approach with the fixed background gradients, the steady temperature and density profiles in the power balanced state can be predicted by using the so-called flux matching technique [11, 18]. A way of evaluating the prediction accuracy is to measure the deviation between actual gradients observed in the experiment and the input gradient values reproducing the experimental turbulent fluxes in the simulation. For instance, let $P_{\text{i(sim)}} = P_{\text{i(sim)}}(L_{T_{\text{i}}}^{-1}, L_{T_{\text{e}}}^{-1}, L_{n_{\text{e}}}^{-1})$, $P_{\text{e(sim)}} = P_{\text{e(sim)}}(L_{T_{\text{i}}}^{-1}, L_{T_{\text{e}}}^{-1}, L_{n_{\text{e}}}^{-1})$, and $\Gamma_{\text{e(sim)}} = \Gamma_{\text{e(sim)}}(L_{T_{\text{i}}}^{-1}, L_{T_{\text{e}}}^{-1}, L_{n_{\text{e}}}^{-1})$ be the calculated ion and electron energy and particle fluxes, respectively, as nonlinear functions of the ion-, electron-temperature, and density gradients, where the other equilibrium parameters are fixed. Then, the temperature- and density-gradient variations ($\Delta L_{T_{\text{i}}}^{-1}$, $\Delta L_{T_{\text{e}}}^{-1}$, $\Delta L_{n_{\text{e}}}^{-1}$) are determined by the following flux matching relations for the ions and electrons,

$$P_{\text{i(sim)}}(L_{T_{\text{i(EXP)}}}^{-1} + \Delta L_{T_{\text{i}}}^{-1},\ L_{T_{\text{e(EXP)}}}^{-1} + \Delta L_{T_{\text{e}}}^{-1},\ L_{n_{\text{e(EXP)}}}^{-1} + \Delta L_{n_{\text{e}}}^{-1}) = P_{\text{i(EXP)}}\ , \tag{10}$$

$$P_{\text{e(sim)}}(L_{T_{\text{i(EXP)}}}^{-1} + \Delta L_{T_{\text{i}}}^{-1},\ L_{T_{\text{e(EXP)}}}^{-1} + \Delta L_{T_{\text{e}}}^{-1},\ L_{n_{\text{e(EXP)}}}^{-1} + \Delta L_{n_{\text{e}}}^{-1}) = P_{\text{e(EXP)}}\ , \tag{11}$$

$$\Gamma_{\text{e(sim)}}(L_{T_{\text{i(EXP)}}}^{-1} + \Delta L_{T_{\text{i}}}^{-1},\ L_{T_{\text{e(EXP)}}}^{-1} + \Delta L_{T_{\text{e}}}^{-1},\ L_{n_{\text{e(EXP)}}}^{-1} + \Delta L_{n_{\text{e}}}^{-1}) = \Gamma_{\text{e(EXP)}}\ , \tag{12}$$

where the subscript "(EXP)" means the nominal experimental values. Note that Eqs. (10) – (12) are a set of nonlinear coupled equations for ($\Delta L_{T_{\text{i}}}^{-1}$, $\Delta L_{T_{\text{e}}}^{-1}$, $\Delta L_{n_{\text{e}}}^{-1}$). But, one can reduce them to a linearized form, i.e.,

$$\begin{pmatrix} \Delta L_{T_{\text{i}}}^{-1} \\ \Delta L_{T_{\text{e}}}^{-1} \\ \Delta L_{n_{\text{e}}}^{-1} \end{pmatrix} = \begin{pmatrix} \dfrac{\partial P_{\text{i(sim)}}}{\partial L_{T_{\text{i}}}^{-1}} & \dfrac{\partial P_{\text{i(sim)}}}{\partial L_{T_{\text{e}}}^{-1}} & \dfrac{\partial P_{\text{i(sim)}}}{\partial L_{n_{\text{e}}}^{-1}} \\ \dfrac{\partial P_{\text{e(sim)}}}{\partial L_{T_{\text{i}}}^{-1}} & \dfrac{\partial P_{\text{e(sim)}}}{\partial L_{T_{\text{e}}}^{-1}} & \dfrac{\partial P_{\text{e(sim)}}}{\partial L_{n_{\text{e}}}^{-1}} \\ \dfrac{\partial \Gamma_{\text{e(sim)}}}{\partial L_{T_{\text{i}}}^{-1}} & \dfrac{\partial \Gamma_{\text{e(sim)}}}{\partial L_{T_{\text{e}}}^{-1}} & \dfrac{\partial \Gamma_{\text{e(sim)}}}{\partial L_{n_{\text{e}}}^{-1}} \end{pmatrix}^{-1} \begin{pmatrix} \Delta P_{\text{i}} \\ \Delta P_{\text{e}} \\ \Delta \Gamma_{\text{e}} \end{pmatrix}\ , \tag{13}$$

where $\Delta P_{\text{i}} \equiv P_{\text{i(EXP)}} - P_{\text{i(sim)}}$, $\Delta P_{\text{e}} \equiv P_{\text{e(EXP)}} - P_{\text{e(sim)}}$, and $\Delta \Gamma_{\text{e}} \equiv \Gamma_{\text{e(EXP)}} - \Gamma_{\text{e(sim)}}$. Actually, the coefficient matrix is evaluated in the similar way to Figs. 9(a) – 9(c). In the previous work in Ref. [11], the ion heat flux is adjusted by only the ion temperature gradient parameter, so that the electron heat flux still deviates from the experimental one. For more precise treatments, one needs to consider the 3×3 matrix approach shown in Eqs. (10) – (13), resulting from the coupling among the heat and particle fluxes at each radial position, but the accurate experimental evaluation of the particle flux is necessary.

In the present study, since the there are no experimental data for Γ_e as mentioned in Sec. 4.2, the multiple flux matching technique is applied to the GKV simulation results (shown in Figs. 7) such that the radial profiles of P_i and P_e simultaneously match the experimental ones, i.e.,

$$P_{i(sim)}(L_{T_{i(EXP)}}^{-1} + \Delta L_{T_i}^{-1},\ L_{T_{e(EXP)}}^{-1} + \Delta L_{T_e}^{-1}) = P_{i(EXP)}\ , \tag{14}$$

$$P_{e(sim)}(L_{T_{i(EXP)}}^{-1} + \Delta L_{T_i}^{-1},\ L_{T_{e(EXP)}}^{-1} + \Delta L_{T_e}^{-1}) = P_{e(EXP)}\ . \tag{15}$$

Note that although the linearized form with matrix coefficient in Eq. (13) provides one the lowest order evaluation of $(\Delta L_{T_i}^{-1}, \Delta L_{T_e}^{-1})$ as shown in Figs. (9), the present multiple flux matching based on Eqs. (14) and (15) takes into account their nonlinear dependencies. Figures 10(a) and 10(b) show the flux matching results for the ion and electron energy fluxes, respectively. The temperature-gradient variations for each radial position are summarized in Tab. 2, where $P_{s=i,e(matched)}$ means the GKV simulations results with $(L_{T_{i(EXP)}}^{-1} + \Delta L_{T_i}^{-1},\ L_{T_{e(EXP)}}^{-1} + \Delta L_{T_e}^{-1})$. One finds that the experimental fluxes are well reproduced except for the ion flux in the outer region of $\rho > 0.58$, where the prediction error for the ion- and electron-temperature gradients for $\rho \leqslant 0.58$ is evaluated as less than $\pm 30\%$. In the outer region, the weak dependence on the temperature-gradient shown in Fig. 9(c) prevents the flux matching within $\pm 30\%$ range of $(\Delta L_{T_i}^{-1}, \Delta L_{T_e}^{-1})$. Besides, the density-gradient validations of $\pm 15\%$ from the experimental value (shown in Tab. 2) indicate that the ion and electron energy fluxes are roughly proportional to $L_{n_e}^{-1}$ (or η_e^{-1}), e.g., $P_i = 0.399$ at $-15\% L_{n_e}^{-1}$ and $P_i = 0.668$ at $+15\% L_{n_e}^{-1}$ (shown by the 9th and 10th rows in Tab. 2), where $\eta_e \simeq 2$ at $\rho = 0.76$ in the present case. The similar characteristic in the density-gradient dependence for $\eta_e > 1$ has also been found in Ref. [34].

Since it has been confirmed that the significant zonal flow generation in the TEM turbulence is related to the transport suppression in the outer region [cf. Fig. 6(b)], the turbulence simulation without zonal flow generations can provide us with useful insights, where the result is shown in the last row in Tab. 2. Then, we see that the simulation results on both the ion and electron energy fluxes are strongly affected by the existence of zonal flows, and the transport shortfall in the ion flux becomes less significant. This is an artificial treatment, but clearly suggests the importance of the accurate zonal flow treatment in the simulation model. Actually, the generation of TEM-driven zonal flows and its impact on the turbulent transport show quite strong dependence on the equilibrium parameters $(R/L_{T_e}, T_e/T_i,$ etc.) as shown in Refs. [35, 36], and have not fully been clarified yet. Also, collisions with impurities from the wall and divertor and/or the toroidal magnetic field ripple, which are ignored in the present simulation model, may lead to relatively stronger zonal flow damping in the outer region. Some global effects of the radial propagation of the heat flux and the turbulence intensity [8, 37, 38] can also influence the zonal flow dynamics.

5. Summary

In this paper, quantitative comparisons of the ion and electron heat transport between gyrokinetic simulation and JT-60U tokamak experiment are carried out by using a local

Table 2. Temperature-gradient variations in multiple flux matching for P_i and P_e

ρ	$\Delta L_{T_i}^{-1}/L_{T_i(EXP)}^{-1}$	$\Delta L_{T_e}^{-1}/L_{T_e(EXP)}^{-1}$	$P_{i(matched)}$	$P_{i(EXP)}$	$P_{e(matched)}$	$P_{e(EXP)}$
0.30	-15%	+15%	0.299	0.274	0.177	0.208
0.40	-10%	+ 0%	0.464	0.490	0.348	0.338
0.50	+10%	-30%	0.735	0.743	0.545	0.503
0.58	+20%	-30%	0.823	0.891	0.681	0.645
0.66	+20%	-20%	0.581	0.972	0.783	0.789
0.66	+15%	+ 0%	0.516	0.972	0.929	0.789
0.76	+0%	+30%	0.625	0.973	1.044	0.986
0.76	+15%	+ 0%	0.613	0.973	0.695	0.986
0.76(w/ -15% in $L_{n_e}^{-1}$)	+ 0%	+ 0%	0.399	0.973	0.581	0.986
0.76(w/ +15% in $L_{n_e}^{-1}$)	+ 0%	+ 0%	0.668	0.973	1.002	0.986
0.76(w/o ZF)	+0%	+0%	1.192	0.973	1.353	0.986

gyrokinetic code GKV incorporating realistic magnetic geometry and fully-gyrokinetic electrons, where the ITG- and/or TEM-driven turbulent transport and zonal flow generations are investigated. In order to examine the prediction capability of the flux-tube gyrokinetic simulations, an L-mode plasma with sufficiently small ρ^* ($\sim$ 1/500) is chosen for the quantitative comparisons, where the mean radial electric field and its shearing effect are also negligibly small. Nonlinear ITG and/or TEM simulations by GKV with kinetic electrons successfully reproduce the radial profiles of the ion and electron energy fluxes which are relevant to the experimental values in the core region, whereas the adiabatic-electron case indicates relatively larger deviations. It is revealed that the zonal flow generation in the outer region ($\rho > 0.58$) with TEM-dominated turbulence is much more significant than that in the core region with ITG- and ITG-TEM-dominated turbulence ($\rho \leqslant 0.58$). Then, the transport shortfall for the ion energy flux appears in the outer region.

Extending the conventional ion heat flux matching with adjusting a single parameter of the ion temperature gradient, we performed a multiple flux matching for both the ion and electron energy fluxes. The temperature-gradient variations giving the matched energy fluxes in the core region are simultaneously determined for ions and electrons with the prediction error less than ±30%, while the weak temperature-gradient dependence of turbulent transport and zonal flows in the the outer region prevents the flux matching. The turbulence simulation without the TEM-driven zonal flows indicates the strong influence of both the ion and electron energy fluxes, where the ion transport shortfall becomes less significant.

For further improvement of the prediction accuracy of gyrokinetic simulations and also constructing a credible reduced transport model, one needs the quantitative comparison of the particle flux between detailed experimental measurements and turbulence simulations. Also, more detailed analyses of the zonal flow dynamics are required, including its generation and damping mechanisms associated with the collisions with impurities, the toroidal magnetic field ripple, and some global effects such as the radial propagation of the heat flux and

the turbulence intensity. As the fluctuation measurements in JT-60U L-mode plasmas is available only for the very edge region, direct comparisons of the turbulence spectrum with the experimental measurement is out of scope at present, but they will be addressed for other appropriate experimental set-up in future works.

Acknowledgments

References

 [1] A. J. Brizard and T. S. Hahm, Rev. Mod. Phys. 79, 421 (2007)
 [2] H. Sugama and W. Horton, Phys. Plasmas 5, 2560 (1998)
 [3] X. Garbet, Y. Idomura, L. Villard, and T. -H. Watanabe, Nucl. Fusion 50, 043002 (2010)
 [4] Y. Idomura, T. -H. Watanabe, H. Sugama, C. R. Physique 7, 650 (2006)
 [5] J. Candy and R. E. Waltz, Phys. Rev. Lett. 91, 045001 (2003)
 [6] R. E. Waltz, J. Candy, and C. C. Petty, Phys. Plasmas 13, 072304 (2006)
 [7] B. F. McMillan, X. Lapillonne, S. Brunner, L. Villard *et al.*, Phys. Rev. Lett. 105, 155001 (2010)
 [8] M. Nakata and Y. Idomura, Nucl. Fusion 53, 113039 (2013)
 [9] C. Holland, A. E. White, G. R. McKee, M. W. Shafer *et al.*, Phys. Plasmas 16, 052301 (2009)
[10] T. L. Rhodes, C. Holland, S. P. Smith, A. E. White *et al.*, Nucl. Fusion 51, 063022 (2011)
[11] T. Görler, A. E. White, D. Told, F. Jenko *et al.*, Phys. Plasmas 21, 122307 (2014)
[12] J. Chowdhury, W. Wan, Y. Chen, S. E. Parker *et al.*, Phys. Plasmas 21, 112503 (2014)
[13] D. Told, F. Jenko, T. Görler, F. J. Casson *et al.*, Phys. Plasmas 20, 122312 (2013)
[14] N. T. Howard, A. E. White, M. Greenwald, M. L. Reinke *et al.*, Phys. Plasmas 20, 032510 (2013)
[15] M. Nunami, T. -H. Watanabe, and H. Sugama, Phys. Plasmas 20, 092307 (2013)
[16] A. Ishizawa, T. -H. Watanabe, H. Sugama, M. Nunami *et al.*, Nucl. Fusion 55, 043024 (2015)
[17] R. V. Bravenec, J. Candy, M. Barnes, and C. Holland, Phys. Plasmas 18, 122505 (2011)
[18] J. Candy, C. Holland, R. E. Waltz, M. R. Fahey *et al.*, Phys. Plasmas 16, 060704 (2009)
[19] R. E. Waltz and C. Holland, Phys. Plasmas 15, 122503 (2008)
[20] M. Nakata, T. -H. Watanabe, H. Sugama, Phys. Plasmas 19, 022303 (2012)
[21] S. Maeyama, Y. Idomura, T. -H. Watanabe, M. Nakata *et al.*, Phys. Rev. Lett. 113 255002 (2015)
[22] Y. Asahi, A. Ishizawa, T. -H. Watanabe, H. Sugama *et al.*, Plasma Fusion Res. 10, 1403047 (2015)
[23] T. -H. Watanabe and H. Sugama, Nucl. Fusion 46, 24 (2006)
[24] M. Nakata, A. Matsuyama, N. Aiba, S. Maeyama *et al.*, Plasma Fusion Res. 9, 1403029 (2014)
[25] N. Hayashi and JT-60 Team, Phys. Plasmas 17, 056112 (2010)

[26] M. Honda, S. Ide, T. Takizuka, N. Hayashi *et al.*, Nucl. Fusion 53 073050 (2013)

[27] A. Lenard and I. B. Bernstein, Phys. Rev. 112, 1456 (1958)

[28] N. Miyato, Y. Kishimoto, and J. Q. Li, Plasma Phys. Control. Fusion 48, A335 (2006)

[29] H. Sugama, T. -H. Watanabe, and M. Nunami, Phys. Plasmas 16, 112502 (2009)

[30] K. Tani, M. Azumi, H. Kishimoto, and S. Tamura, J. Phys. Soc. Jpn. 50, 1726 (1981)

[31] M. Yoshida, Y. Koide, H. Takenaga, H. Urano *et al.*, Plasma Phys. Control. Fusion 48, 1673 (2006)

[32] S. Toda, M. Nunami, A. Ishizawa, T. -H. Watanabe *et al.*, J Phys Conf Ser. 561, 012020 (2014)

[33] G. M. Steabler, J. E. Kinsey and R. E. Waltz, Phys. Plasmas 14, 055909 (2007)

[34] D. R. Ernst, J. Lang, W. M. Nevins, M. Hoffman *et al.*, Phys. Plasmas 16, 055906 (2009)

[35] J. Lang, Y. Chen, and S. E. Parker, Phys. Plasmas 14, 082315 (2007)

[36] J. Lang, S. E. Parker, and Yang Chen, Phys. Plasmas 15, 055907 (2008)

[37] Y. Idomura, H. Urano, N. Aiba, and S. Tokuda, Nucl. Fusion 49, 065029 (2009)

[38] S. Yi, J. M. Kwon, P. H. Diamond, and T. S. Hahm, Nucl. Fusion 55, 092002 (2015)
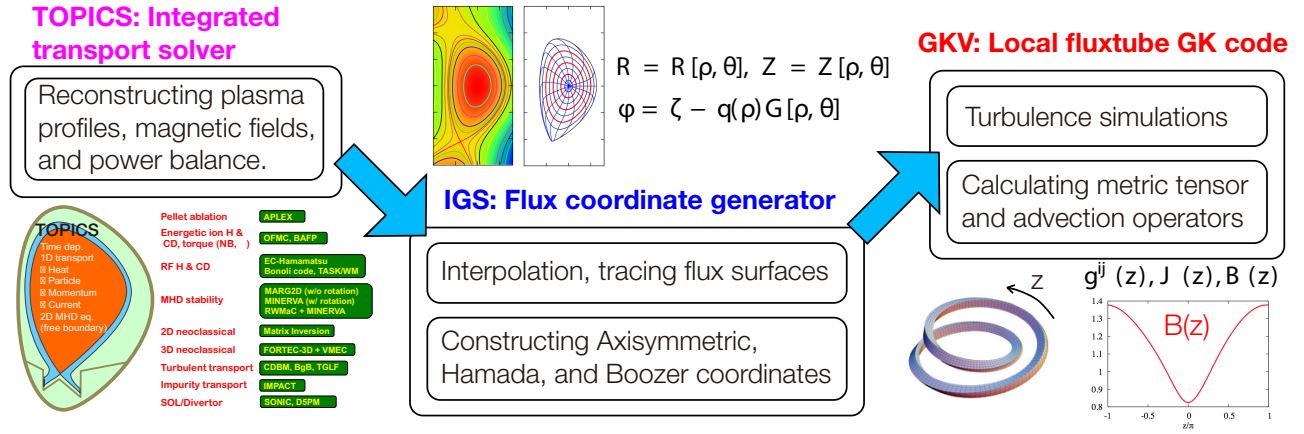
Figure 1. Data-flow of the experimental MHD equilibrium produced by the integrated transport solver TOPICS to the gyrokinetic solver GKV via the flux coordinate generator IGS.
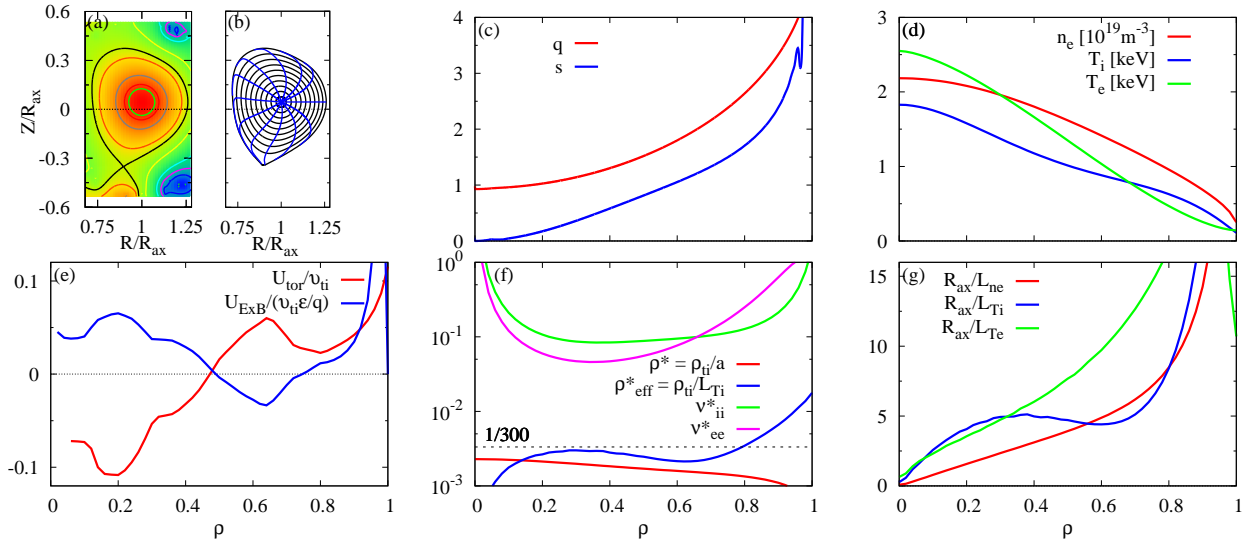
Figure 2. Equilibrium in JT-60U L-mode (#E45072). (a) Poloidal cross-section of the plasma, (b) Constructed straight-field-line (Boozer) coordinates, (c) Safety-factor and magnetic-shear $[(\rho/q)(dq/d\rho)]$ profiles, (d) Density and temperature profiles, (e) Toroidal- and poloidal-rotation profiles, (f) Normalized gyroradius and collisionality profiles, (g) Normalized density- and temperature-gradient profiles.
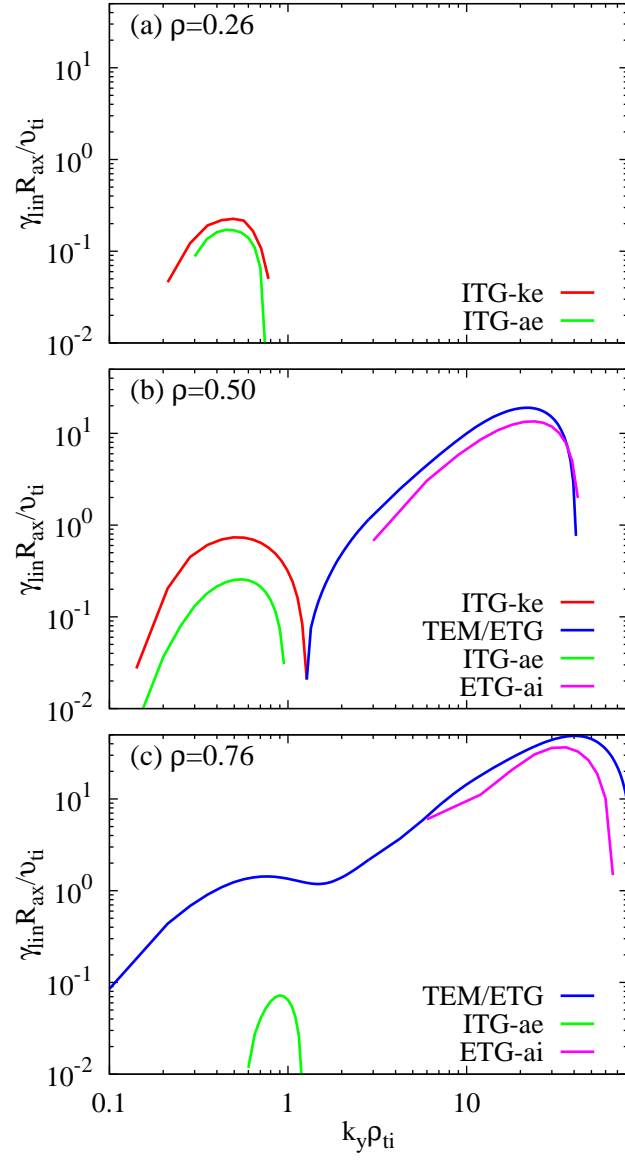
Figure 3. The wavenumber spectra of the linear-mode growth rates $\gamma_{\text{lin}}(k_y)$ at (a) $\rho = 0.26$, (b) $\rho = 0.50$, and (c) $\rho = 0.76$, where "ke", "ae", and "ai" stand for kinetic electrons, adiabatic electrons, and adiabatic ions, respectively.
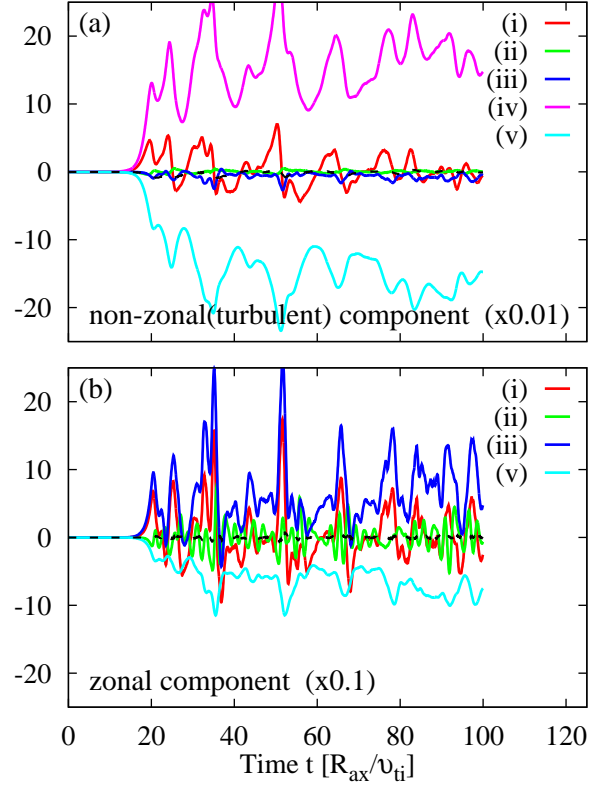
Figure 4. Time evolution of the entropy balance for (a) non-zonal and (b) zonal components at $\rho = 0.50$, where the labeling number of each line corresponds to the term in the left hand side of Eqs. (8) and (9), respectively, and the dashed line shows the deviation from the exact balance.
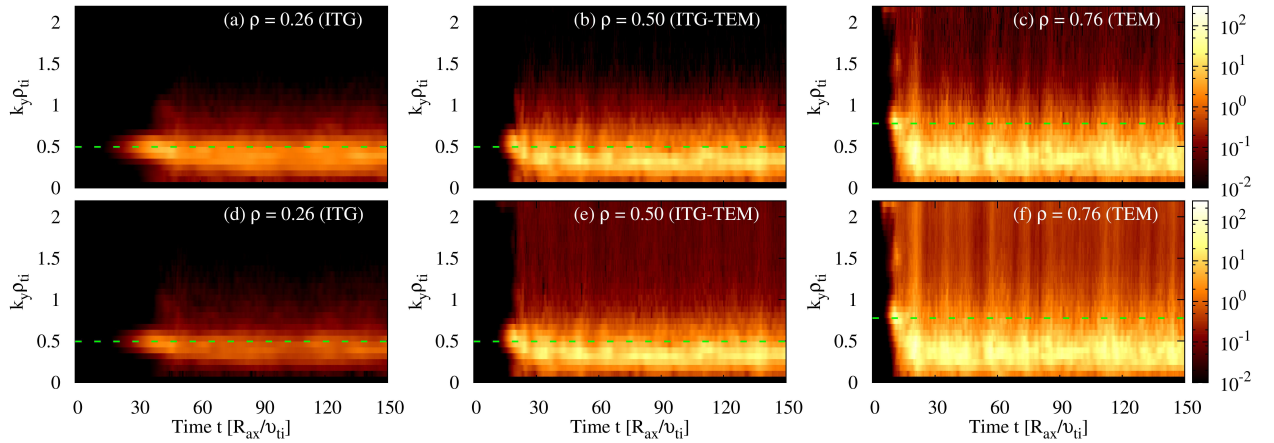
Figure 5. Temporal evolutions of the wavenumber spectra in the turbulent ion and electron energy flux density, $Q_{ik_\perp}/Q_{\mathrm{GBi}}$ [(a) – (c)] and $Q_{ek_\perp}/Q_{\mathrm{GBi}}$ [(d) – (f)], at $\rho = 0.26$, 0.50, 0.76, $\rho = 0.50$. The wavenumber giving the maximum linear growth rate within $k_y\rho_{\mathrm{ti}} \leqslant 2.0$ is indicated by the horizontal dashed line.
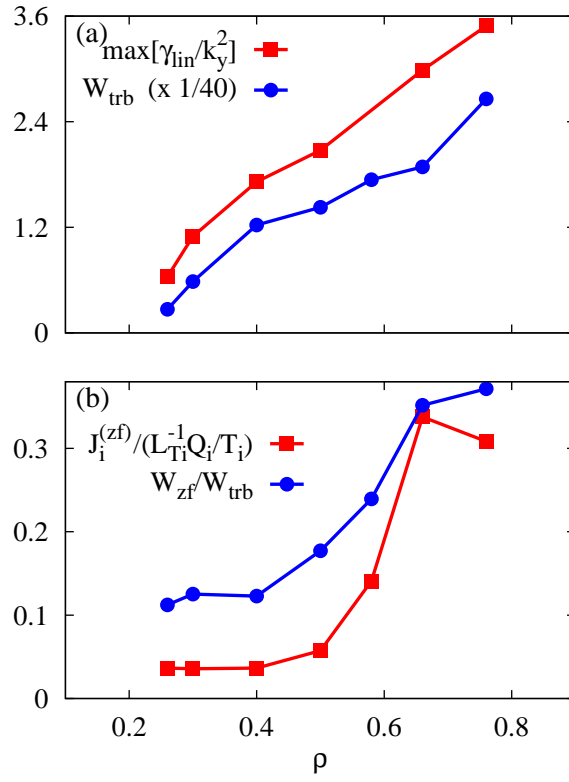
Figure 6. Radial profiles of (a) the mixing-length estimate of diffusivity $\max[\gamma_{\mathrm{lin}}/k_y^2]$ and the turbulence energy W_{trb} in the gyro-Bohm unit, (b) the normalized entropy transfer rate for zonal modes $\mathcal{J}_i^{(\mathrm{zf})}/(L_{T_i}^{-1} Q_i/T_i)$ and the zonal flow energy normalized by the turbulence one $W_{\mathrm{zf}}/W_{\mathrm{trb}}$.
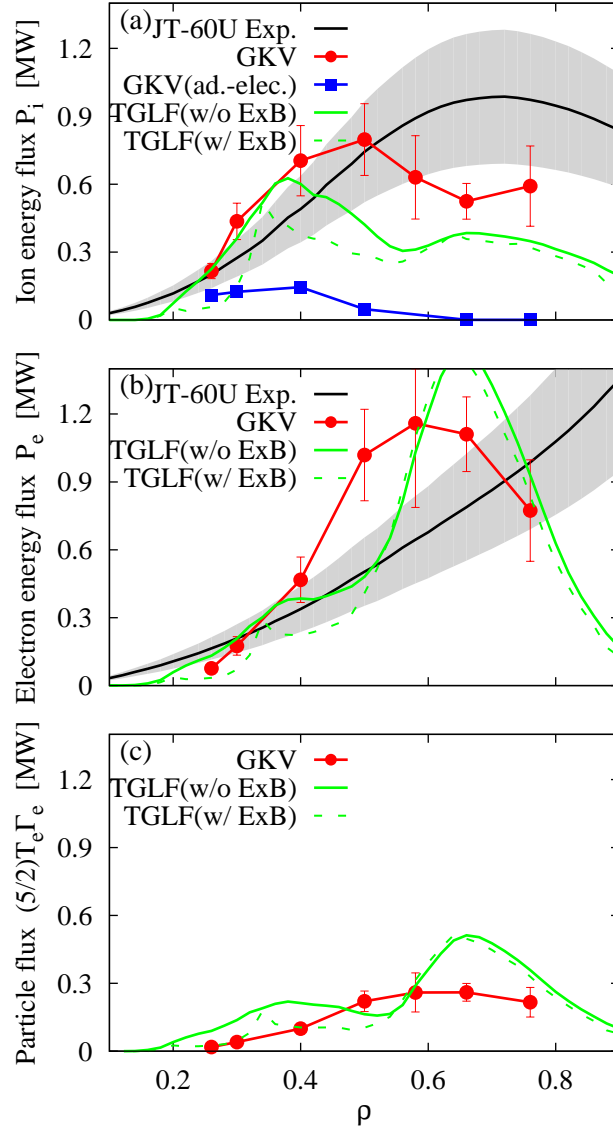
Figure 7. Comparison of the radial profiles of (a) ion energy flux P_i, (b) electron energy flux P_e, and (c) convective part in the electron energy flux (i.e., particle flux) $(5/2)T_e\Gamma_e$ against the experimental results, where the results with the adiabatic-electron ("ad.-elec.") approximation and with a gyrofluid-based transport model TGLF(with and without the mean-$E\times B$ shear) are also plotted. The hatched region shows the experimental measurement error.
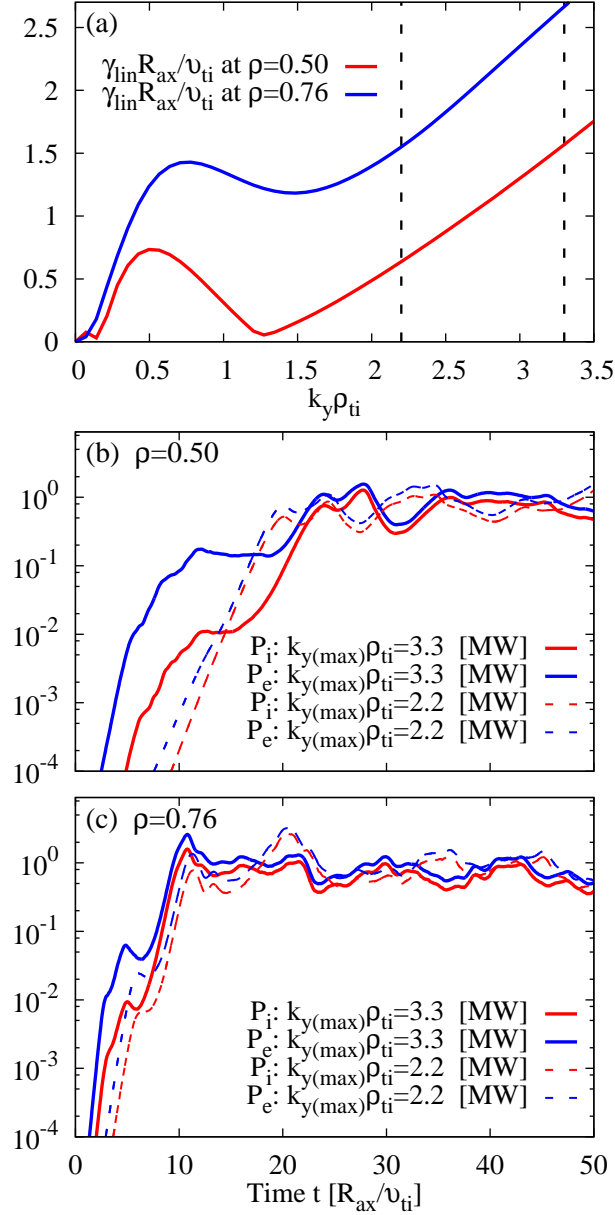
Figure 8. (a) Linear growth rates at $\rho = 0.50$ and $\rho = 0.76$. Convergence check with respect to $k_{y(\text{max})}$ on (b) ITG-TEM-driven energy fluxes at $\rho = 0.50$ and (c) TEM-driven energy fluxes at $\rho = 0.76$.
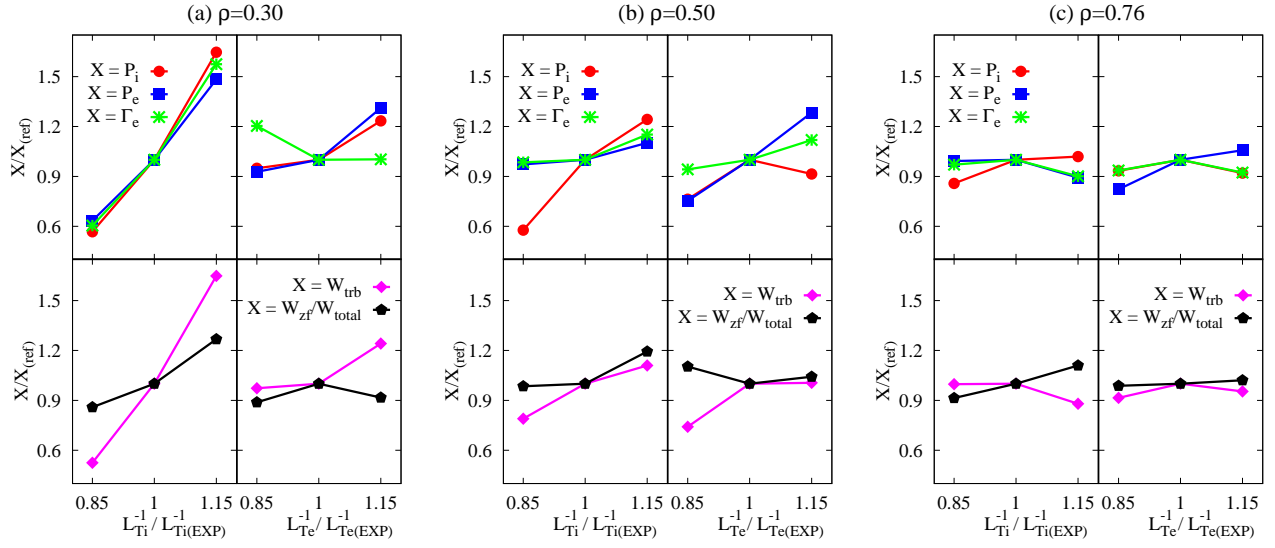
Figure 9. $L_{T_i}^{-1}$- and $L_{T_e}^{-1}$-scans for the ion energy flux (P_i), the electron energy flux (P_e), the turbulence energy (W_{trb}), and the zonal flow energy normalized by the total one (W_{zf}/W_{total}) at (a) $\rho = 0.30$, (b) $\rho = 0.50$, and (c) $\rho = 0.76$, where the other parameters are fixed in each scan.
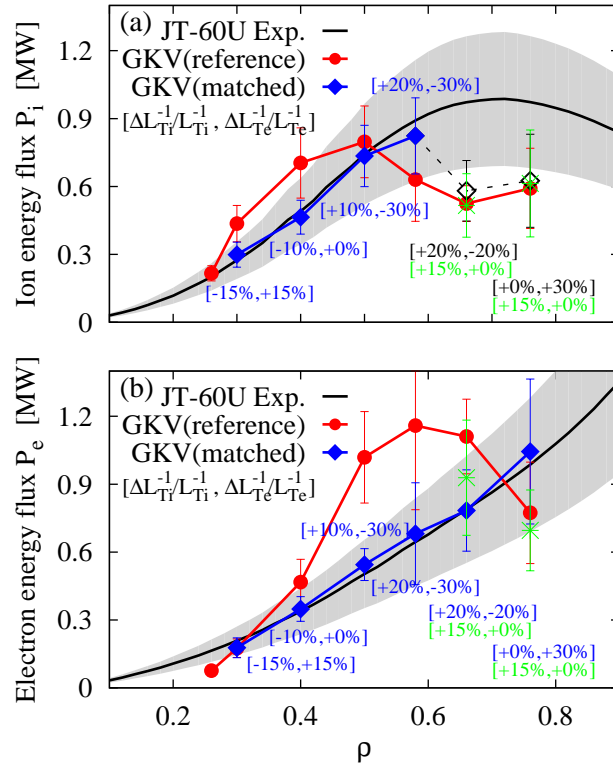

Figure 10. Flux-matching results on (a) the ion energy flux P_i and (b) the electron energy flux P_e with the modified L_{T_i} and L_{T_e}, where the open diamond and star symbols show the cases that the flux matching is prevented by the weak L_{T_i} and L_{T_e} dependencies.